LAL 04-115
October 2004

Angular patterns of interferometric detectors and resonant bars for tensorial and scalar gravitational waves

Nicolas Arnaud, Monica Varvella

Laboratoire de l'Accélérateur linéaire
CNRS-IN2P3 et Université de Paris-Sud, Bât. 200, B.P. 34, 91898 Orsay Cedex (France)

Abstract

Among the main challenges of gravitational wave (GW) data analysis, the non-uniformity of current GW detector responses is a major concern. Indeed, it strongly limits the efficiency of any network of GW antennas, even though such configurations are mandatory to separate true GW signals from noise fluctuations. This article just aims at giving a complete analytical description of GW detector antenna patterns. Most of its contents can be found elsewhere in the literature, but we thought useful to collect them in a single place with additional details, in order to provide an understanding as complete as possible of this essential basic feature of any GW network data analysis. The two main types of GW detectors – interferometers and resonant bars – are considered in this article, as well as both tensorial and scalar GW, the former predicted by the General Relativity while the later occurs in alternative theories of gravity.

1 Introduction

Analyzing properly the data provided by GW detectors is as difficult and complex as the experimental work aiming at operating these instruments at their best sensitivities with the highest duty cycle. GW signals occur at random times with waveforms a priori unknown, which makes compulsory the use of several filtering techniques in parallel to try not to miss any of these rare events.
In addition to these computing challenges (algorithm design, management of large computer farms, selection of potentially interesting events...), another problem makes the analysis even more complex: the spatial response of current GW detectors is not uniform. Indeed, it depends on the relative position of the antenna with respect to the source location [1]. Therefore, the GW amplitudes associated to the same signal can be very different in distant detectors, which makes more difficult – and never 100% efficient – any network analysis using outputs from several antenna. Yet, such methods are compulsory to validate a real event with a satisfying confidence level – see e.g. [2, 3, 4, 5, 6, 7, 8, 9] – as a single detector cannot easily separate real GW from random noise fluctuations.
This article aims at summarizing the main features of the antenna patterns of current GW detectors: interferometers and resonant masses. In both cases, two types of GW are considered: GW generated in the General Relativity framework (tensorial GW) and scalar GW predicted by alternative theories of gravity – see [10] and references therein for a review of these theories. In particular, as an original contribution to this topic, the analytical form of the interferometer antenna pattern for scalar GW is computed.

2 Geometrical aspects and notations

To describe the effect of a GW on the spatial metric, let us start with its 'proper frame' defined in Figure 1 for details. The GW propagates along the third axis of the frame, while the two first are chosen aligned with the induced perturbations, located in the transverse plane.

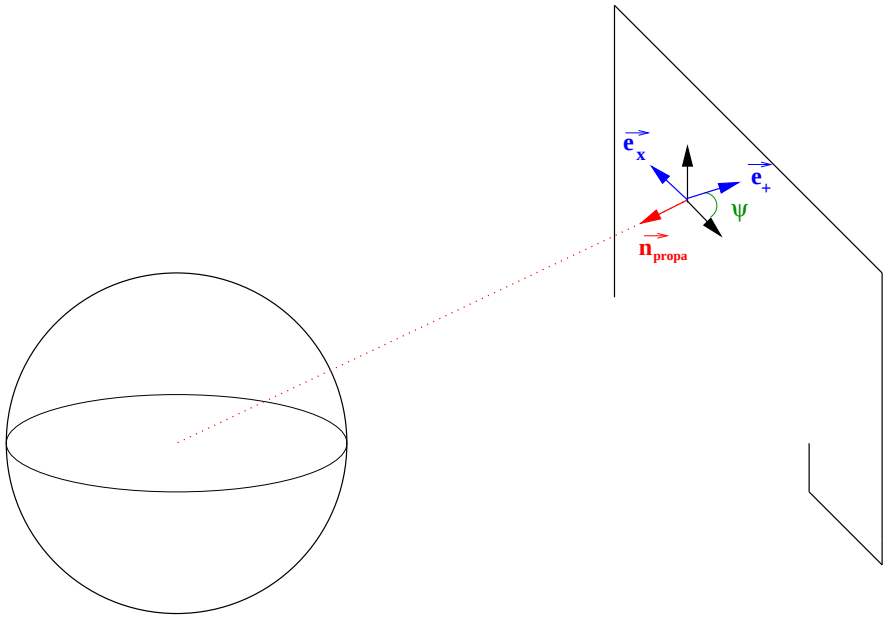

Figure 1: GW local frame in which the GW tensor can be simply written. The angle ψ is an additional degree of freedom, taking into account rotations of the frame around the source-Earth line.

In General Relativity, a GW is described in the Transverse-Traceless gauge by two time-dependent polarizations: h_+ et $h_\times$. In its proper frame, the tensor measuring the spatial perturbation induced by the GW is simply:

$$H_{\rm GR} = \begin{pmatrix} h_+ & h_\times & 0 \\ h_\times & -h_+ & 0 \\ 0 & 0 & 0 \end{pmatrix} \tag{1}$$

Adding a GW scalar component b to the two tensorial ones simply requires to change the two non-zero diagonal terms of the tensor: $h_+ \to (h_+ + b)$ and $-h_+ \to (-h_+ + b)$. One gets:

$$H_{\rm scalar} = \begin{pmatrix} h_+ + b & h_\times & 0 \\ h_\times & -h_+ + b & 0 \\ 0 & 0 & 0 \end{pmatrix} \tag{2}$$

Now, to compute antenna patterns, one needs to move from the GW proper frame to Earth-based frames associated to GW detectors. A first degree of freedom is visible in Figure 1: let $\vec{n}_{\rm propa}$ be the unit vector pointing from the GW source to Earth; the GW proper axis –

located in the plane perpendicular to this direction – are defined through a rotation angle ψ – the polarization angle – around $\vec{n}_{\rm propa}$.
The position of the source in the sky is monitored by three angles: two recording its location in a fixed frame, plus a phase taking into account the Earth proper rotational motion. The most convenient choice is to use the 'equatorial frame' as its third direction is aligned with the Earth rotation axis; in this frame, a source is labeled by its right ascension α (a 'longitude') and its declination δ (a 'latitude'), both shown in Figure 2.

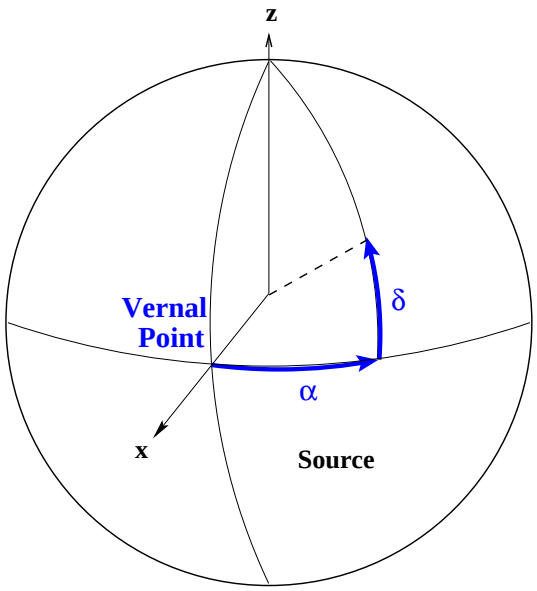

Figure 2: Definition of the equatorial frame: the third direction of the frame 'z' is aligned with the Earth rotational axis while the first one, 'x', points toward the vernal point.

Detector positions on Earth are labeled by their latitudes l and their longitudes L (positive west-wards by convention). For detectors having privileged directions like interferometers and resonant masses, additional angles are required – see below and Figure 3 for the definition of these local angles.

- For an interferometer, two angles are mandatory: the angle χ between the two arms – it will be shown that $\chi = 90^\circ$ is optimal – and a angle γ, monitoring the local orientation of the antenna on Earth. By convention, γ is chosen to be the angle between the local South-North direction and the interferometer arm bisecting line, counted counterclockwise. Table 1 summarizes these informations for the first generation of large-scale interferometers.
- For resonant bars, one angle is sufficient to describe the bar local orientation. In this case, ρ is defined as the angle between the South-North local direction and the bar axis, counted counterclockwise again. Table 2 contains geographical informations needed to describe the resonant bars currently operated.

Finally, the local hour angle $\mathfrak{H}(t)$ is mandatory to take into account the detector motion with respect to the celestial sphere due to Earth proper rotation. For a source of right ascension α and a detector of longitude L, it is defined as:

$$\mathfrak{H}(t) \;=\; \kappa t \;+\; T_{\mathrm{Greenwich}}(0) \;-\; (\alpha \,+\, L) \tag{3}$$

with $T_{\mathrm{Greenwich}}(0)$ being the Greenwich sidereal time at 0h UT and $\kappa \approx 1.0027379 \times 15^{\circ}/\mathrm{hour}$, as a sidereal day lasts approximately 23 hours and 56 minutes.

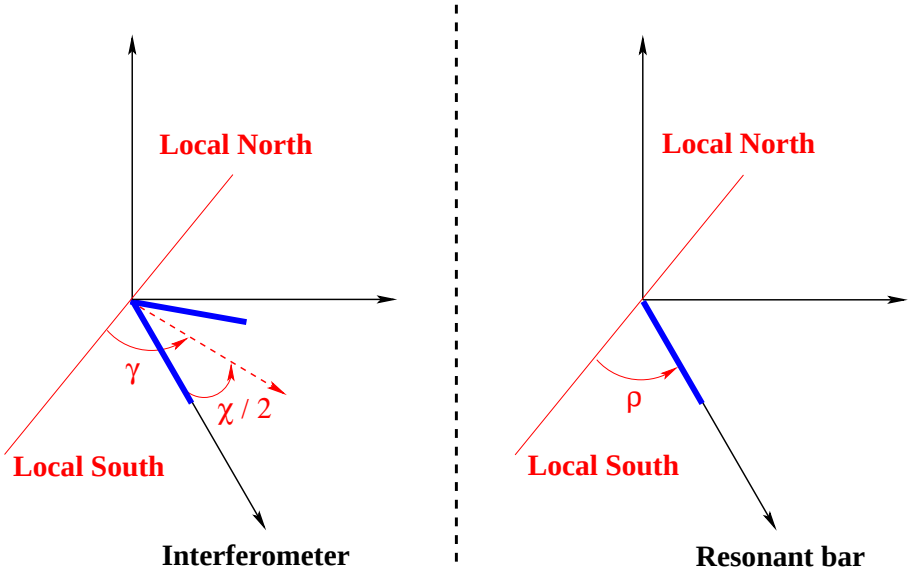

Figure 3: Description of GW detector local orientations.

Detector	Latitude l (°)	Longitude L (°)	χ (°)	γ (°)
ACIGA [11]	-31.4	-115.7	90.0	*Not decided*
GEO600 [12]	52.3	-9.8	94.3	158.8
LIGO Hanford [13]	46.5	119.4	90.0	261.8
LIGO Livingston [13]	30.6	90.8	90.0	333.0
TAMA300 [14]	35.7	-139.5	90.0	315.0
Virgo [15]	43.6	-10.5	90.0	206.5

Table 1: Interferometer locations on Earth

Detector	Latitude l (°)	Longitude L (°)	ρ (°)
ALLEGRO [16]	30.5	-268.8	40.0
AURIGA [17]	45.4	-12.0	136.0
EXPLORER [18]	46.5	-6.2	141.0
NAUTILUS [19]	41.8	-12.7	136.0
NIOBE [20]	-31.9	-115.8	0.0

Table 2: Resonant bar location on Earth

3 Interferometer pattern

A GW detector is sensitive to a linear combination $h(t)$ of the different GW polarizations:

$$h(t) \;=\; \underbrace{F_+(t)\,h_+(t) \;+\; F_\times(t)\,h_\times(t)}_{\text{General Relativity tensorial GW}} \;+\; \underbrace{F_b(t)\,b(t)}_{\text{Scalar GW}} \tag{4}$$

The weighting factors F_+, $F_\times$ and F_b are called antenna pattern functions. To compute them analytically, one needs to transport the GW perturbation tensor from the GW frame to the detector local frame. Using the angles introduced in the previous section, this transformation can be split into three rotations: GW proper frame $\rightarrow$ celestial sphere frame $\rightarrow$ frame centered on the detector $\rightarrow$ detector local frame. If P is the full transformation matrix, the GW perturbation matrix M expressed in the detector local frame is equal to:

$$M \;=\; {}^tP \;\times\; H \;\times\; P \tag{5}$$

The antenna pattern functions are finally computed from the M matrix coefficients, using a formula which depends on the type of GW detector considered.

3.1 Tensorial GW

Let $\vec{n}_1$ and $\vec{n}_2$ be unit vectors along the interferometer arms; the interaction between the GW and the antenna can be written [3]:

$$h \;=\; \frac{1}{2}\left({}^t\vec{n}_1 \cdot M \cdot \vec{n}_1 \;-\; {}^t\vec{n}_2 \cdot M \cdot \vec{n}_2 \right) \tag{6}$$

with M the GW perturbation tensor defined above in Eq. (5). After extensive calculations, the final form of the 'General Relativity' antenna pattern functions F_+ and $F_\times$ is given by [3, 8, 21]:

$$\begin{pmatrix} F_+ \\ F_\times \end{pmatrix} = \sin\chi \begin{pmatrix} \cos 2\psi & \sin 2\psi \\ -\sin 2\psi & \cos 2\psi \end{pmatrix} \begin{pmatrix} a \\ b \end{pmatrix} \tag{7}$$

with

$$\begin{aligned}
a = \;& -\; \frac{1}{16}\sin 2\gamma\,(3 \,-\, \cos 2l\,)\,(3 \,-\, \cos 2\delta\,)\cos 2\mathfrak{H} \;-\; \frac{1}{4}\cos 2\gamma\,\sin l\,(3 \,-\, \cos 2\delta\,)\sin 2\mathfrak{H} \\
& -\; \frac{1}{4}\sin 2\gamma\,\sin 2l\,\sin 2\delta\,\cos\mathfrak{H} \;-\; \frac{1}{2}\cos 2\gamma\,\cos l\,\sin 2\delta\,\sin\mathfrak{H} \\
& -\; \frac{3}{4}\sin 2\gamma\,\cos^2 l\,\cos^2\delta \\
b = \;& -\; \cos 2\gamma\,\sin l\,\sin\delta\,\cos 2\mathfrak{H} \;+\; \frac{1}{4}\sin 2\gamma\,(3 \,-\, \cos 2l\,)\,\sin\delta\,\sin 2\mathfrak{H} \\
& -\; \cos 2\gamma\,\cos l\,\cos\delta\,\cos\mathfrak{H} \;+\; \frac{1}{2}\sin 2\gamma\,\sin 2l\,\cos\delta\,\sin\mathfrak{H}
\end{aligned}$$

Looking at the previous expressions, one can note that the dependence in the ψ and χ angles are factorized: the polarization angle ψ simply introduces a rotation of the antenna pattern, while the F coefficients are clearly maximal for orthogonal arms. The a and b functions have no particular physical meaning: their distributions differ from one interferometer to the other. On the other hand, the combination $\sqrt{a^2+b^2}$ has a unique distribution for all detectors, see Section 4.

3.2 Scalar GW

For a scalar GW, the antenna pattern function is computed by following exactly the same procedure. Original calculations give:

$$F_b \;=\; \frac{\sin\chi}{2}\;\left[\,K_s\,\sin 2\gamma \;+\; K_c\,\cos 2\gamma\,\right] \tag{8}$$

with

$$\begin{aligned} K_s &= \sin^2\mathfrak{H}\,\cos^2\delta \;-\; \sin^2 l\,\cos^2\delta\,\cos^2\mathfrak{H} \;-\; \cos^2 l\,\sin^2\delta \;+\frac{1}{2}\,\sin 2\lambda\,\sin 2\delta\,\cos\mathfrak{H} \\ K_c &= \sin l\,\cos^2\delta\,\sin 2\mathfrak{H} \;+\; \cos l\,\sin 2\delta\,\sin\mathfrak{H} \end{aligned}$$

Like for tensorial GW, $\sin\chi$ is a scaling factor for the interferometer response, coming directly from Eq. (6) and the local orientation angle γ dependence is factorized. But the most important feature here is that F_b does not depend on the polarization angle ψ.

4 Interferometer antenna pattern interpretation

To understand the shapes of these antenna pattern functions, it is interesting to re-express them in a particular frame, shown in Figure 4; its two first axis are along the detector arms, thus assumed to be perpendicular, which is the case for all interferometers apart GEO600 which exhibits only a small deviation from this optimal situation – see Table 1. These expressions are simple enough to explain the main features of the interferometer patterns.
Using the spherical angles introduced in Figure 4, one gets:

$$F_+ \;=\; \frac{1}{2}\,(\,1\,+\,\cos^2\theta\,)\,\cos(2\phi)\,\cos(2\psi) \;-\; \cos\theta\,\sin(2\phi)\,\sin(2\psi) \tag{9}$$

$$F_\times \;=\; \frac{1}{2}\,(\,1\,+\,\cos^2\theta\,)\,\cos(2\phi)\,\sin(2\psi) \;+\; \cos\theta\,\sin(2\phi)\,\cos(2\psi) \tag{10}$$

$$F_b \;=\; \frac{1}{2}\,\sin^2\theta\,\cos(2\phi) \tag{11}$$

The expressions for F_+ and $F_\times$ are well-known – for instance, they can be found in Ref. [1] – and present the same structures than Eq. (7). It is clear that $F_{+,\times}$ and F_b are very different. First, $|F_b| \leq 1/2$, which means that at best 50% of the scalar GW amplitude can be recovered in an interferometer. This feature strongly limits the potential of such antennas for the detection of scalar signals.
On the other hand, F_+ and $F_\times$ can reach ± 1; extremizing them requires $\cos\theta = \pm 1$, i.e. a GW perpendicular to the interferometer plane – on the other hand, for these directions, $F_b = 0$.

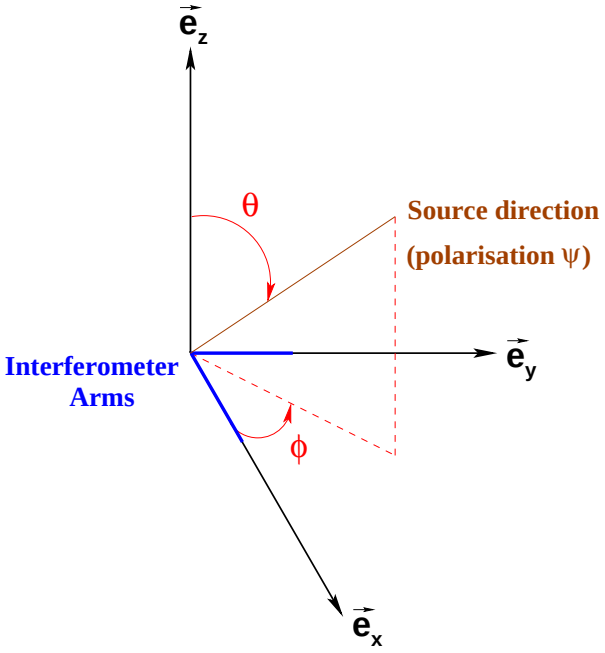

Figure 4: Interferometer local frame: its two first directions are aligned with the detector arms (assumed to be perpendicular) and spherical coordinates (θ, ϕ) are introduced.

One can also note that F_+ and $F_\times$ are zero in four directions belonging to the interferometer plane, defined by $(\cos 2\phi = 0)$: along the arm bisecting line and in the perpendicular direction. As F_+ and $F_\times$ depend on the polarization angle ψ, they have a zero mean in any direction of the sky. Therefore, still following Ref. [8], one introduces the ψ-independent quantity $\overline{F}$ to quantify the strength of the interferometer pattern in a given direction:

$$\overline{F} \;=\; \sqrt{\frac{F_+^2 \;+\; F_\times^2}{2}} \tag{12}$$

The squares ensure a non-cancellation of terms; while the square root reduces $\overline{F}$ to a quantity homogeneous to a GW amplitude – the meaningful quantity for what concerns GW detection. Finally, the factor $1/\sqrt{2}$ is simply a convention 'averaging' the two squared terms, validated below when interpretations of $\overline{F}$ will be given. From Eq. (7), it is clear that $\sqrt{F_+^2 \;+\; F_\times^2}$, the norm of the vector $(F_+, F_\times)$, is a ψ-independent quantity. Indeed, one has:

$$\sqrt{F_+^2 \;+\; F_\times^2} \;=\; |\,\sin\chi\,|^2\;\sqrt{a^2 \;+\; b^2} \tag{13}$$

The previous equation explains why the distribution of the quantity $\sqrt{a^2+b^2}$ has a physical meaning. In the following, the two quantities $\overline{F}$ (ranging from 0 to $1/\sqrt{2}$ for perpendicular arms) and $|F_b|$ will be used to compare tensorial and scalar antenna patterns. The mean value of $\overline{F}$ is nothing but the common RMS of the antenna patterns F_+ and $F_\times$, which have 0-mean due to their ψ-dependence.

5 Viewing GW antenna patterns: the sky maps

A convenient way to visualize the antenna pattern of GW detectors is to use two-dimensional density plots, the sky maps [3, 8]. Any direction in the sky is located by a couple of coordinates – $(\phi, \cos\theta)$ or $(\alpha, \sin\delta)$ depending on the chosen frame[1] – and the antenna pattern amplitude is represented by a color code. As a first example, Figure 5 shows $\overline{F}$ and $|F_b|$ in the interferometer local frame – $(\phi, \cos\theta)$. All features mentioned in the previous section are clearly visible.

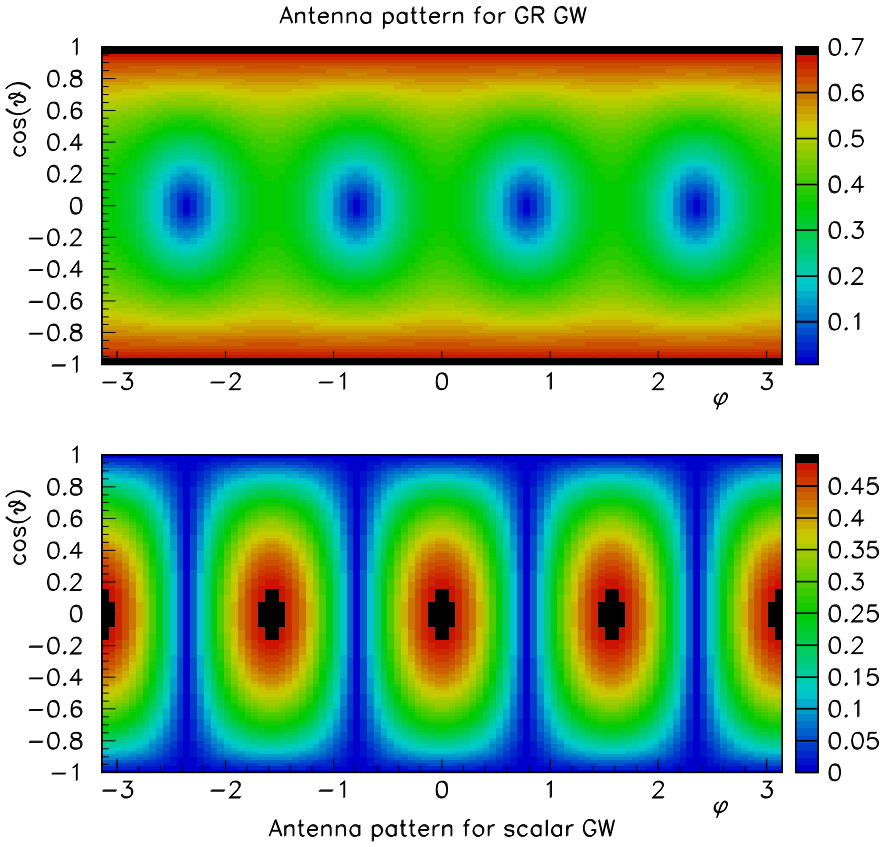

Figure 5: Antenna pattern comparison in the interferometer local frame $(\phi, \cos\theta)$: top plot, tensorial pattern; bottom plot, scalar pattern. $\overline{F}$ has four zeros in the interferometer plane (incoming wave along the arm bisecting line) and is maximal for normal incidence. On the other hand, $|F_b|$ is maximal for GW coming along one arm and null for GW perpendicular to the antenna.

In this particular frame, the antenna patterns look 'repetitive'. To see more 'attractive' pictures, one can recompute the same diagrams in a general frame, independent from any interferometer. This change modifies the pattern shapes, but not their characteristics.
Therefore, now labeling the source position by the couple $(\alpha, \sin\delta)$, the Virgo antenna pat-

[1] In both cases, the second variable is not the angle itself but rather its sine, in order to get a uniform coverage of the celestial sphere.

terns[2] – for tensorial and scalar GW – are shown in Figure 6. The two crosses show the directions perpendicular to the interferometer plane, represented by the curved dashed line.

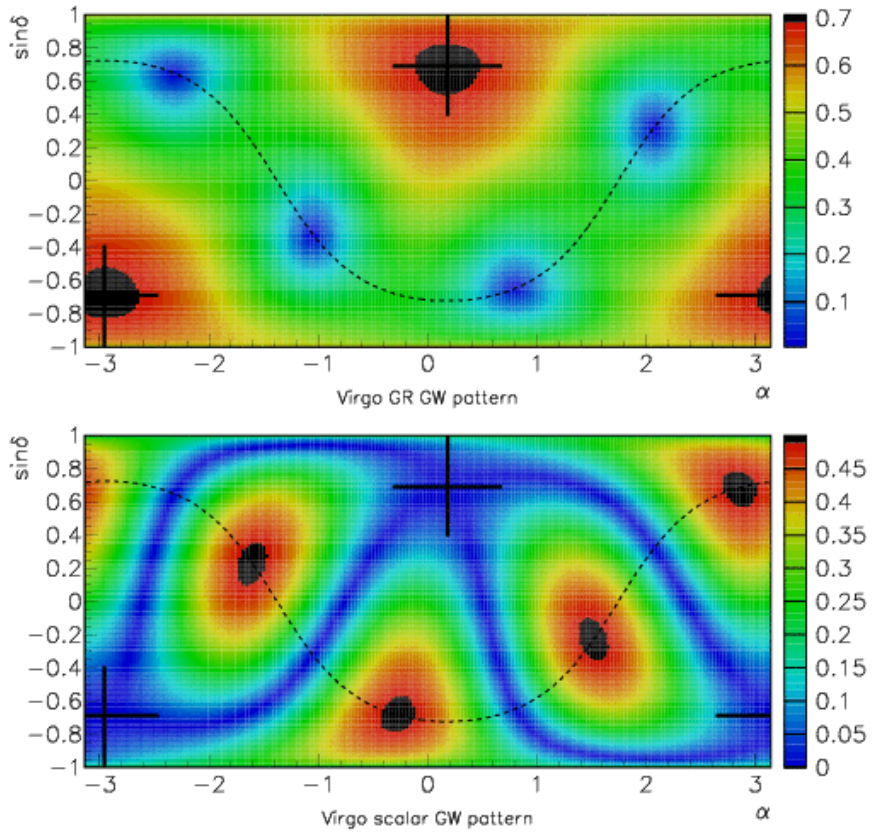

Figure 6: GW antenna pattern $(\alpha, \sin\delta)$ for the Virgo detector. The two marks show the directions perpendicular to the detector plane, represented by the dashed line. In this way, one can check that the two diagrams present the expected features, already visible in Figure 5.

To conclude on interferometer pattern sky maps, Figures 7 and 8 compare the antenna patterns of the six first generation interferometers, for tensorial and scalar GW respectively. For both plots, the local orientation of ACIGA has been chosen in order to optimize its contribution to a full-sized network including all interferometers, assumed to have identical sensitivities. This corresponds to $\gamma_{\mathrm{ACIGA}} \approx 0°$ – modulo 90° due to the γ-dependence of all antenna patterns.
A last way to compare tensorial and scalar antenna patterns is to compute their probability distributions, assuming a uniform distribution of sources in the sky.
Results are shown in Figure 9: both distributions have zero mean; the F_b plot sharply peaks around zero while the $F_{+,\times}$ distribution – identical for F_+ and $F_\times$ as expected – is approximately flat between -0.5 and 0.5, before decreasing on the edges of the plot.

[2]To compute such antenna patterns, the origin of the angle α is chosen arbitrarily – indeed, at a given sidereal time, Earth proper motion leads to a horizontal shift of the pattern by a phase $\kappa t + T_{\mathrm{Greenwich}}(0)$. The important point to ensure a proper comparison between various interferometers is that all sky maps are computed using the same origin for α.

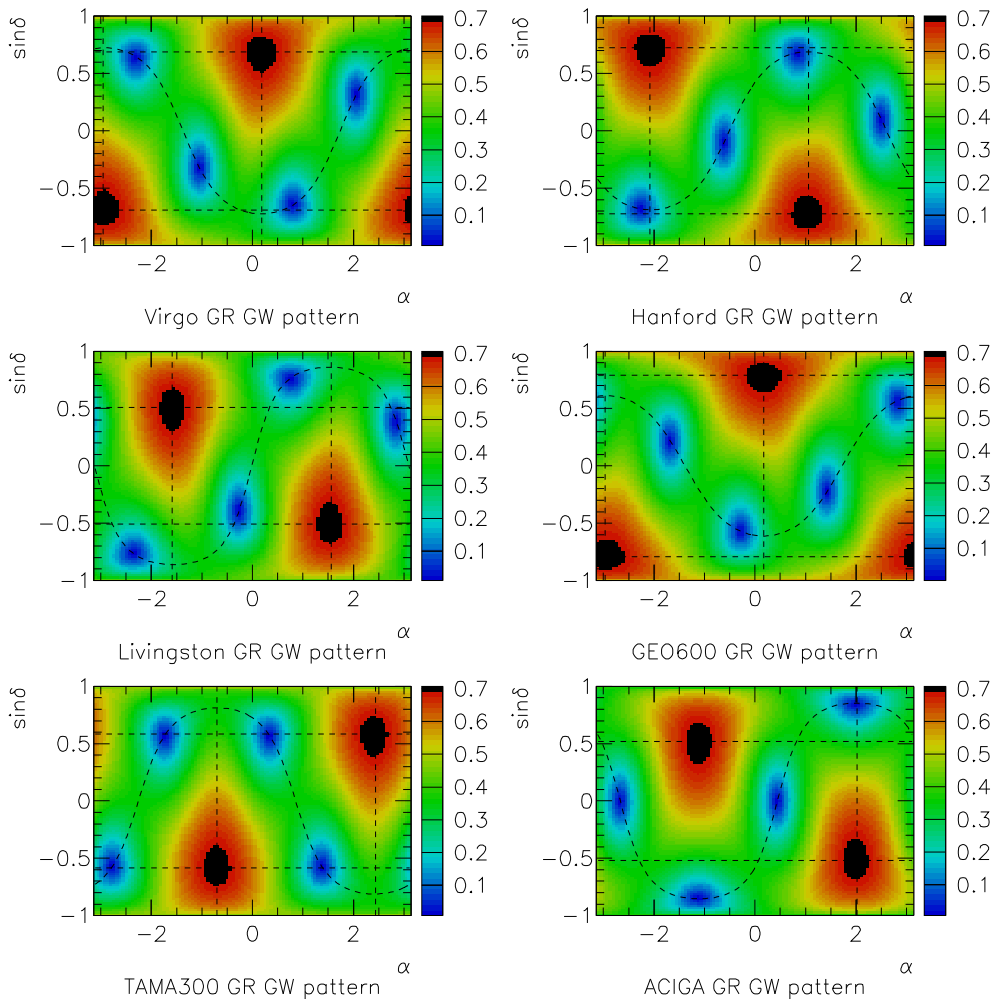

Figure 7: First generation interferometer antenna patterns for tensorial GW. The dashed straight lines cross each other in the two directions perpendicular to the interferometer plane – for which the antenna response is optimal – while the curved dashed line shows the location of the interferometer plane in which are located the four blind directions for such detectors.

6 Resonant bar pattern

The same procedure can be applied to resonant bars to compute their antenna patterns. Due to the bar axisymmetrical shape, the three functions F_+, $F_\times$ and F_b are found to be proportional to $\sin^2(\theta_{\rm pol})$, where $\theta_{\rm pol}$ is the polar angle with respect to the bar axis. Therefore, one can see immediately that directions perpendicular to the bar are strongly favored, while the resonant mass is blind along its axis. Indeed, let us define two angular functions:

$$A_{\rm bar} = \cos\rho \sin l \sin\mathfrak{H} + \sin\rho \cos\mathfrak{H} \quad (14)$$

$$B_{\rm bar} = \cos\rho \sin l \sin\delta \cos\mathfrak{H} + \cos\rho \cos l \cos\delta - \sin\rho \sin\delta \sin\mathfrak{H} \quad (15)$$

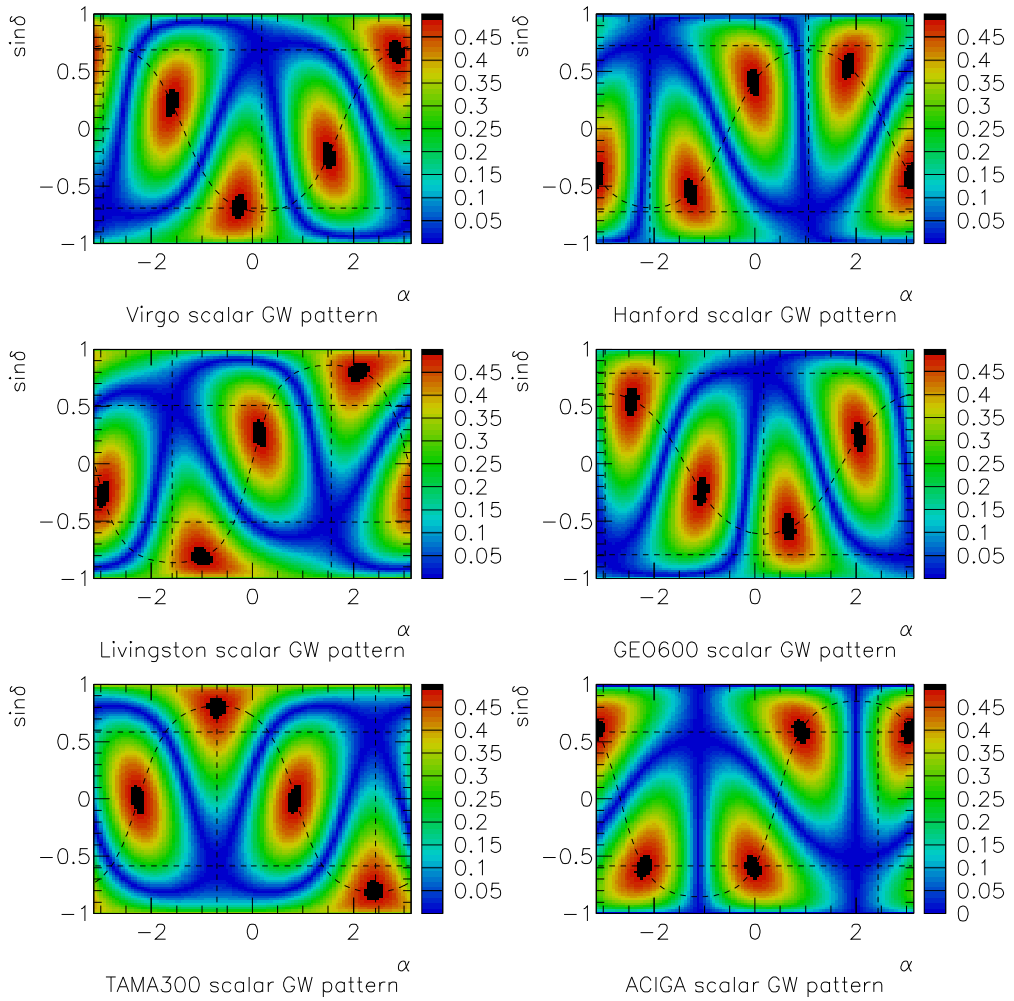

Figure 8: First generation interferometer antenna patterns for scalar GW. As expected, directions perpendicular to the detector plane are blind, while optimal responses are found along the arms, thus shifted from 45° with respect to the blind directions for tensorial GW.

In term of these variables, the bar pattern functions are the following:

$$F_+ = \left[A_{\rm bar}^2 - B_{\rm bar}^2 \right] \cos 2\psi + 2\, A_{\rm bar}\, B_{\rm bar} \sin 2\psi \tag{16}$$

$$F_\times = 2\, A_{\rm bar}\, B_{\rm bar} \cos 2\psi - \left[A_{\rm bar}^2 - B_{\rm bar}^2 \right] \sin 2\psi \tag{17}$$

$$\Rightarrow \overline{F} = \frac{A_{\rm bar}^2 + B_{\rm bar}^2}{\sqrt{2}} \tag{18}$$

$$F_b = A_{\rm bar}^2 + B_{\rm bar}^2 = \sqrt{2}\, \overline{F} = \sin^2 \left(\theta_{\rm pol} \right) \tag{19}$$

The previous equations show that for resonant bars, the knowledge of $\overline{F}$ – indeed proportional to the sine squared of the polar angle – is sufficient to describe all antenna patterns, both for tensorial and scalar GW. In addition, like for interferometers, the scalar antenna pattern is

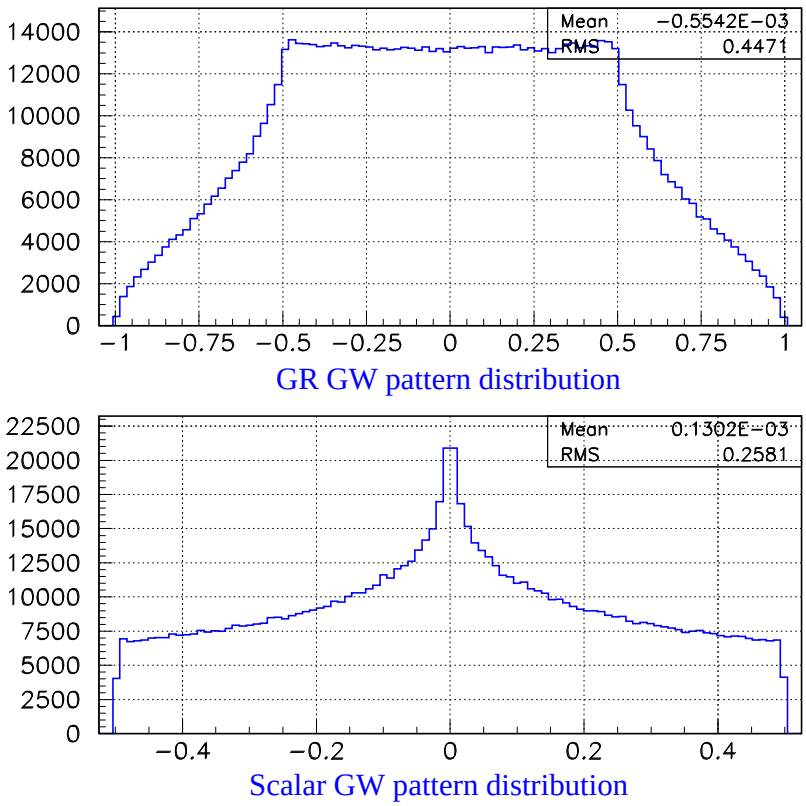

Figure 9: General Relativity and scalar GW pattern distributions, assuming a uniform distribution of sources in the sky: α and ψ uniform in $[-\pi;\pi]$ and $\sin\delta$ uniform in $[-1;1]$. Both distributions have zero mean and their RMS – equal to the mean values of $\overline{F}$ – are respectively $1/\sqrt{5}$ (tensorial GW) and $1/\sqrt{15}$ (scalar GW). Vertical scales are arbitrary.

independent from the polarization angle ψ. Yet, F_b is not bounded by ± 0.5 but can reach ± 1 in case of optimal orientation of the source: at equal sensitivities, bars appear more suitable than interferometers for the detection of scalar GW.
As predicted by Eq. (19), the distribution of $\overline{F}$ has the same shape as the distribution of a sine squared whose cosine is uniform between -1 and 1 – see Figure 10. It peaks at its maximal value which is reached on a great circle in the sky.
Finally, Figure 11 compares the antenna patterns of the five bars currently running. Contrary to interferometers – cf. Figures 7 or 8 –, the bars are almost aligned to optimize the performances of the network they form; therefore, their antenna patterns are very similar. As expected from the dependence on $\sin^2(\theta_{\rm pol})$ previously mentioned, a bar is optimally sensitive to GW perpendicular to its axis and blind along it. These patterns are valid both for tensorial and scalar GW.

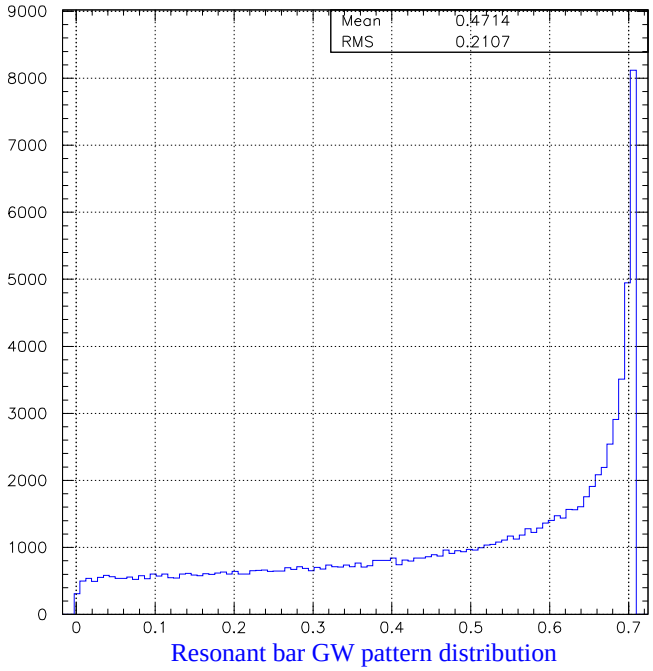

Figure 10: Distribution of $\overline{F}$ for a resonant bar, assuming a uniform distribution of sources in the sky. As expected, it has the same shape as the distribution of a sine squared whose cosine is drawn uniformly between -1 and 1. Its mean value – which is also the RMS of the zero-mean functions F_+ and $F_\times$ – is equal to $\sqrt{2}/3$.

7 Conclusion

The antenna patterns of interferometers and resonant bars have been analytically computed in this article, both for tensorial and scalar GW. They are clearly non uniform on the celestial sphere and in addition they depend on the types of detector such as on the GW radiation considered. Interferometer antenna patterns are more complicated than resonant bar shapes, which exhibit an axisymmetry. The latter detectors appear more suitable to search for scalar GW waves, provided that they can reach the same sensitivities than interferometers and that the GW emission is mostly located in the resonant bar sensitivity frequency range.
In the future, this situation may evolve with the introduction of spherical resonant detectors. Indeed, these have various advantages with respect to resonant bars – see e.g. [22] – : in particular, their response is independent from the source location and from the GW polarization! In addition, using a single detector, one can merge information coming from the five quadrupole modes and from the monopole mode of the sphere to fully reconstruct the GW tensor and the source location in the sky... This inverse problem has been solved in the presence of Gaussian and independent noises in the different sensors, either using a maximum likelihood method [23] or only linear algebra [24]. Prototypes of such generators [25, 26, 27] are currently being developed worldwide.

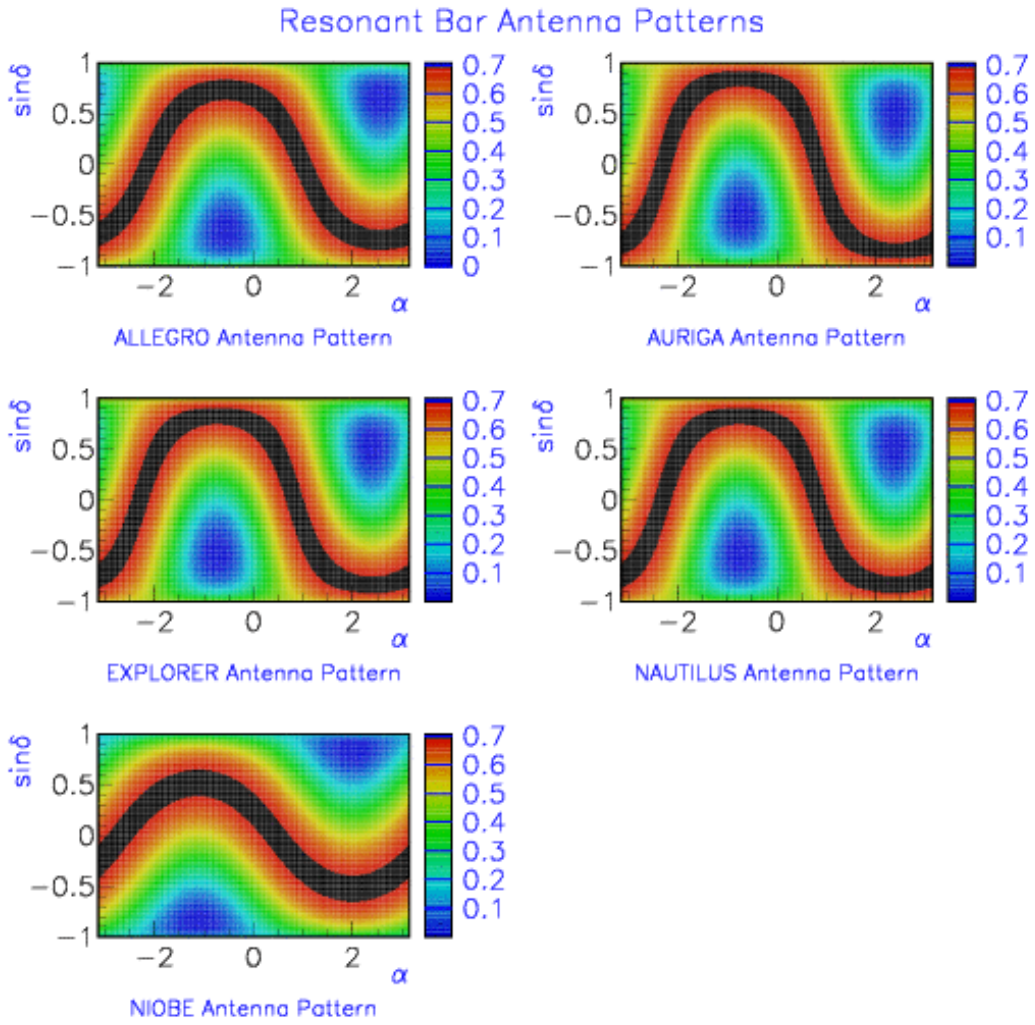

Figure 11: Comparison of the resonant bar antenna patterns. They are all similar as the five resonant bars are almost parallel. One can also note that they have their better sensitivity for GW perpendicular to their axis and that they are blind for GW parallel to it. These plots are valid both for tensorial and scalar GW.

Acknowledgment

The authors would like to thank the Orsay Virgo group for their support and fruitful comments.

References

[1] K.S. Thorne, *Gravitational Radiation*, in **300 Years of Gravitation**, S.W.Hawking and W.Israel Editors (Cambridge University Press, 1987).

[2] Y. Gürsel and M. Tinto, *Phys. Rev. D* **40,** 3884 (1989).

[3] P. Jaranowski, A. Krolak, *Phys. Rev. D* **49** 1723 (1994).

[4] L.S. Finn, *Phys. Rev. D* **63** 102001 (2001).

[5] A. Pai, S. Dhurandhar, S. Bose, *Phys. Rev. D* **64** 042004 (2001).

[6] http://igec.lnl.infn.it

[7] Z.A. Allen *et al.*, *Phys. Rev. Lett.* **85** 5046 (2000);
P. Astone *et al.*, *Class. Quantum Grav.* **18** 243 (2001);
P. Astone *et al.*, *Class. Quantum Grav.* **19** 5449 (2002).

[8] N. Arnaud *et al.*, *Phys. Rev. D* **65** 042004 (2002).

[9] N. Arnaud *et al.*, *Phys. Rev. D* **68** 102001 (2003).

[10] M. Varvella, PhD thesis **Gravitational waves in extended gravity: theory and detection**, Universita degli studi di Salerno (2003), available at:
http://www.infn.it/thesis/PS/341-Varvella-dottorato.ps

[11] http://www.anu.edu.au/Physics/ACIGA/

[12] http://www.geo600.uni-hannover.de/

[13] http://www.ligo.caltech.edu/

[14] http://tamago.mtk.nao.ac.jp/

[15] http://www.virgo.infn.it/

[16] http://sam.phys.lsu.edu/ALLEGRO/allegro.html

[17] http://www.auriga.lnl.infn.it/

[18] htttp://www.roma1.infn.it/rog/explorer/

[19] htttp://www.roma1.infn.it/rog/nautilus/

[20] http://www.gravity.pd.uwa.edu.au/publ/niobe.html

[21] P. Jaranowski, A. Krolak, B.F. Schutz, *Phys. Rev. D* **58** 063001 (1998).

[22] W. Johnson, S.M. Merkowitz, *Phys. Rev. Lett.* **70**, 2367 (1993).
J.A. Lobo, *Phys. Rev. D* **52**, 591 (1995).

[23] C. Zhou and P.F. Michelson, *Phys. Rev. D* **51**, 2517 (1995).

[24] S.M. Merkowitz *Phys. Rev. D*, **58**, 062002 (1998).

[25] http://www.das.inpe.br/~graviton/

[26] http://www.minigrail.nl/

[27] http://www.roma1.infn.it/